Large eddy simulations of kagome and body centered cubic lattice cells

Thomas M. Corbett [a],[*], Karen A. Thole [b]

[a] *The Pennsylvania State University, 3127 Research Drive, State College, PA 16801, USA*
[b] *The Pennsylvania State University, State College, PA 16801, USA*

ARTICLE INFO

ABSTRACT

As advanced manufacturing methodologies such as additive manufacturing become accessible and cost effective, more complex and tailored internal cooling schemes can be achieved. One family of cooling geometries that has recently garnered interest within the heat transfer community are lattice structures. These structures offer enhanced mixing and large surface area-to-volume ratios, but their application in advanced heat exchangers is in relative infancy. This study explored the performance of two types of lattice unit cells, specifically Kagome and body centered cubic (BCC), by identifying the flow development and unsteady characteristics using large eddy simulations (LES) at a Reynolds number of 20,000. Simulation results agree well with experimental data, and differences between the two methods was found to be a function of the as-printed quality of the experimental geometry. Results indicate that both lattices feature spatial periodicity in the local Nusselt number and friction factor, due to the changes in flow area and flow interactions in the wake of each lattice strut. LES results show that the flow through the BCC lattice became fully developed, both hydrodynamically and thermally, with fewer unit cells than through the Kagome. In the entry region, the flow in the Kagome lattice became biased towards one side of the channel due to local wakes and interactions with the lattice struts, resulting in a bias to the local heat transfer. The simulations also revealed that the instantaneous vortices shed from the BCC lattice struts interacted with the duct endwalls, pulling the boundary layer from the wall and enhancing heat transfer.

1. Introduction

Heat exchangers are a prevalent part of modern life, with use cases spreading from small electronics cooling to power plants for distributing and dissipating thermal energy. Lattice structures have high surface area-to-volume ratios, making them an ideal candidate for use as a cooling technology. Several studies have recently evaluated lattice structures for cooling in the trailing edge of turbine blades [1,2] and in heat exchangers [3,4].

A lattice is most typically composed of a single "unit" cell in a repeating pattern in both streamwise and spanwise directions. The two most common types of lattice unit cells are triply periodic minimal surfaces (TPMS) that are complex surfaces defined by a mathematical function, or strut-based lattices that are composed of struts arranged in a variety of patterns. While lattice structures have been able to be produced through other means in the past [4], additive manufacturing (AM) opens up the opportunity to implement and curate these features faster and cheaper than was feasible previously.

Several groups in recent years have begun investigations into lattice

structures for cooling applications, featuring both TPMS [5–9] and strut based lattices [2,8,10–27]. Many types of lattice unit cells have been investigated in these studies, with some of the most prominent unit cells including Kagome [2,8,11–14,21–23], body centered cubic (BCC) [8,14, 24–27], face centered cubic (FCC) [8,12,28], cube [1,20], and octet [1, 20]. These unit cells have been investigated in a range of scales, between 10 mm unit cells [1,10] down to 2 mm [8,11]. Additionally, the unit cells have been integrated into test coupons in several ways, including incorporated into channels with various spanwise and streamwise spacings [1,8], as well as used to form a three-dimensional grid [20]. Generally speaking, the thermo-hydraulic performance of lattice structures was greater than that of an empty duct, and have been seen to thermally develop in roughly 3–5 unit cells [14,20]. The specific focus of the current study is on two different unit cell geometries: the BCC and Kagome unit cells.

Recent investigations using Kagome lattice unit cells have leveraged both experimental and steady RANS simulations to explore performance. Hou et al. [29] completed a study on Kagome lattice where the orientation of the geometry was varied. They found that orienting the center struts parallel to flow direction resulted in enhanced heat transfer

---

* Corresponding author.
  E-mail address: Tmc5980@psu.edu (T.M. Corbett).

Nomenclature

A_c	cross-sectional flow area	UC	unit cell size
A_s	surface area	Wchannel width	channel width
D_h	hydraulic diameter, $D_h = 4\frac{A_c}{p}$	x	steamwise position
f	friction factor, $f = \frac{2 \cdot D_h}{\rho \cdot u_{m,in}^2} \cdot \frac{\partial P}{\partial x}$	X	x position as a function of number of unit cells, $X = x/UC$
h	convective heat transfer coefficient, $h = \frac{\dot{m} \cdot c_p \cdot (T_{x,m} - T_{in})}{A_s \cdot \Delta T_{LM}}$	y	spanwise position
H	channel height	Y	y position as a function of number of unit cells, $Y = y/UC$
k	thermal conductivity	z	vertical position
L	channel length	Z	z position as a function of number of unit cells, $Z = z/UC$
L_{center}	width of a unit cell at the midplane location		
n	dominant vortex shedding frequency	*Greek*	
Nu	Nusselt number, $Nu = h \cdot \frac{D_h}{k_{air}}$	$+\Delta x$	dimensionless grid spacing, $+\Delta x = \frac{\Delta x}{\nu \cdot \sqrt{\rho/|\tau_w|}}$
p	channel perimeter	$+\Delta y$	dimensionless grid spacing, $+\Delta y = \frac{\Delta y}{\nu \cdot \sqrt{\rho/|\tau_w|}}$
P	static pressure	$+\Delta z$	dimensionless grid spacing, $+\Delta z = \frac{\Delta z}{\nu \cdot \sqrt{\rho/|\tau_w|}}$
Re	Reynolds number, $Re = \frac{u \cdot D_h}{\nu}$	ε	porosity
St	Strouhal Number, $St = \frac{n \cdot L_{center}}{U}$	ρ	fluid density
T	temperature	ν	kinematic viscosity
T_m	local streamwise mass-averaged temperature	Θ	Non-dimensional temperature, $\theta = \frac{T(x,y,z) - T_{in}}{T_{wall} - T_{in}}$
TI	turbulence Intensity, $TI = \frac{\sqrt{\frac{1}{3}((u')^2 + (v')^2 + (w')^2)}}{u_{m,in}}$	τ_w	wall shear stress
TKE	turbulent kinetic energy, $TKE = 0.5 \cdot ((u')^2 + (v')^2 + (w')^2)$	ωin-plane vorticity	in-plane vorticity
$u_{m,in}$	mass average u-component of velocity at coupon or domain inlet	*Subscripts*	
		in	inlet condition
U	local u-component of velocity	out	outlet condition
		wall	surface condition

performance due to large recirculation zones that occurred between lattice unit cells. This recirculation in the near wall region has been noted by several other researchers as well [8,11,14,22] and was found to be a function of the interactions of the vortices that develop just behind and in front of the lattice struts. The formation of these vortices resulted in a heat transfer bias, where one surface of the lattice design had significantly greater heat transfer than the other, as shown by Liang et al. [14]. There have also been a number of studies that have investigated how changes to the core Kagome geometry impact performance, including modifications to the strut shape [12], length [23], and number impacted the lattice performance [11]. Of these modifications, changes to strut length had the greatest impact on both heat transfer and pressure loss performance, with Kemerli and Kahveci [23] reporting an almost 230 % increase in Nusselt number as unit cell sizes halved and cell porosity increased.

Similar to the Kagome lattice, there has been a significant research effort to better understand the performance of the BCC lattice. Several studies investigated laminar flow through a BCC lattice, and highlighted the impact of porosity [24–26] and developed analytical models to predict heat transfer [27]. Studies by Dixit et al. [24], Takarazawa et al. [25] , and Shahrzadi et al. [26] found that as the porosity of the unit cell decreased, the heat transfer and pressure drop increased considerably. Dixit et al. [24] explained this change in performance to be the result of the increase in surface area increasing the skin friction as well as enabling greater heat transfer. Another study by Ernot et al. [27] developed an analytical model to predict the heat transfer of laminar flow through a BCC lattice, but they found that there were strict limitations on appropriate inlet flow rates, highlighting the difficulty in accurately predicting heat transfer of BCC lattice using simplified models. Two studies by Liang et al. [8,14] investigated turbulent flow through BCC lattice arranged with a streamwise and spanwise spacing similar to a pin fin geometry using experiments and steady RANS simulations. They found in high Reynolds number flows the vortex development in the wake of the BCC lattice resulted in increased average heat transfer on the endwalls relative to the average performance of the

Kagome lattice. Despite the increased heat transfer the measured pressure drop was similar to Kagome lattice, giving rise to a greater thermal efficiency, or relative increase in heat transfer for a given amount of pumping power [14].

While these prior studies have explored many aspects of lattice designs, there is currently no work comparing the unsteady flow features in representative lattice structures, or studies that made of use of higher order modeling techniques beyond steady RANS. The current study expands on the prior work on lattice structure performance by first exploring how the flow develops through subsequent rows of tightly packed Kagome and BCC lattices using experimentally validated large eddy simulations. Additionally, the turbulence generation and underlying transient structures are investigated, and their impact on local heat transfer is described.

2. Computational setup

2.1. Modeling domain and methods

Two forms of lattice unit cells were investigated as part of this study, namely the body centered cubic (BCC) and Kagome lattices, which are shown in Fig. 1(a) and 1(b). Each BCC lattice unit cell had a total of eight struts that were defined such that they connected opposing corners of the cubic unit cell. Each Kagome lattice featured a total of six struts that were defined similarly, though the unit cell shape was hexagonal with a width to height ratio of 3:2, similar to what was used by Parbat et al. [11]. The height of both designs investigated in this study was defined as 1.905 mm, which was a size relevant to a variety of small-scale microchannels previously studied by the authors [30,31]. Because of the aspect ratio of the Kagome lattice, it was slightly wider than the BCC unit cell for this study with an aspect ratio of 1:1. Due to the differences in unit cell shape, the total volume of the Kagome lattice unit cell was physically larger than that of the BCC design. Both of the designs were modeled such that they had a porosity, defined as the empty volume over total unit cell volume, of 75 %. The strut diameter was varied
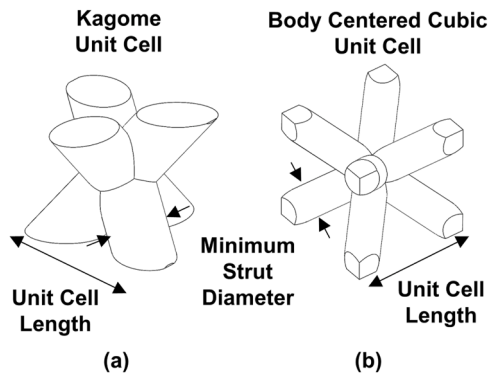
Fig. 1. (a) Kagome and (b) body centered cubic lattice definitions.

between the two designs to maintain this level of porosity as given in Table 1.

The unit cell size was defined as the width of the design, which was 1.91 mm for the BCC unit cell and 2.54 mm for the Kagome unit cell. Unit cells of the respective lattice were arranged into a "core" region, where cells were spaced at exactly one unit cell width, an arrangement which is shown in Fig. 2. For each unit cell type, ten rows of lattice were combined into a "core" region, where the rows were arranged along the flow direction. In addition to the core region, there was an empty entry region, five unit cells in length, and an empty outlet region the length of ten unit cells. The domain was modeled this way to determine if the design of the lattice impacted the flow upstream or downstream of the core region. The two sides of the domain were modeled using a periodic boundary, which in effect captured an infinitely wide duct containing many columns of the lattice designs.

To ensure that the relevant flow features and transient flow dynamics were captured in this simulation, the domain was modeled using Large Eddy Simulations (LES) using a commercial computational fluid dynamics (CFD) solver [32]. The modeled fluid was air, where density was calculated using the ideal gas law and the dynamic viscosity and thermal conductivity were modeled using Sutherland's law. Air entered the domain through a mass flow inlet that imposed an internal Reynolds number of approximately $Re = 21,000$, and air left the domain through a pressure outlet boundary condition. The walls of the domain were set to a constant temperature of 75 °C, and the temperature of the inlet mass flow was set to 23 °C. These conditions were set to mirror an experimental validation that will be discussed Section 2.3. The Wall-Adapting Local Eddy-viscosity (WALE) sub-grid turbulence model was used to capture sub-grid scale turbulence, as it is most appropriate for wall bounded turbulent flows [33]. Time steps were determined such that the Courant number was less than one for the entire domain.

While lattice structures have gained significant interest for applications in conjunction with metal additive manufacturing, the computation model used for this study did not account for the typical surface roughness intrinsic to metal additive components. Modeling the surface

roughness requires significantly more complex meshes or wall models [34,35], which is further exasperated by the variability in metal additive surface roughness. Given the already great computational cost of this analysis due to modeling using LES, the walls in the domain for this study were modeled as smooth.

2.2. Mesh generation and validation

A region of the two meshes that were generated and used for these simulations are shown in Fig. 3(a) and 3(b). Both meshes were generated using the same commercial tool used for modeling, and made use of polyhedral cells. The mesh featured prism layers in order to accurately resolve thermal and velocity gradients in the near wall region with y^+ values of approximately one.

Initial simulations of both geometries were computed using a steady Reynolds averaged Navier Stokes (RANS) simulation. These initial simulations were used in three capacities: to determine the residence time in each domain, to approximate the Taylor micro and Kolmogorov length scales, and to serve as the initial conditions that were used for the LES simulations. The residence time was determined by tracking the amount of time it took an average particle to travel along a streamline from the domain inlet to the domain outlet. The residence time was approximately two milliseconds for both geometries. Estimations of the local Taylor micro and Kolmogorov turbulent length scales were extracted using built in software functions, and the domains were re-meshed such that the cell size fell between these two length scales, as recommended by the software user manual [32]. This remeshing process resulted in an average cell size in the core of the domain of approximately 28.2 μm for both lattices. The final mesh sizes were 13 million cells for the BCC lattice, and 15 million cells for the Kagome lattice. The non-dimensional grid scales $+\Delta x$ and $+\Delta z$ were estimated to be similar for both geometries, with an average value of approximately 50. The non-dimensional y grid scale $+\Delta y$ was one or lower for the entire domain. The re-meshed domains were then run using RANS until they were converged again, and these updated solutions were used as the initial state for the LES simulations.

The first step in determining whether a mesh is sufficiently resolved using LES is to determine the amount of turbulent kinetic energy (TKE) that was explicitly captured as compared to the amount that was modeled using the sub-grid model. The explicitly captured TKE was then compared to the TKE modeled using the sub-grid turbulence model, as recommended by Pope [36]. It was found that the turbulence captured was greater than 99 % for the flow outside of the core mesh region, and greater than 95 % for the vast majority of the flow inside of the core region, indicating that the mesh was well resolved.

As a secondary characterization of the mesh quality, a point was selected downstream of the second row of lattice where significant turbulence generation occurred. A time history of all three components of velocity were recorded at this point for a total of two residence times. Each component of the velocity was then converted into a spectral power density which was then plotted against frequency. An example of

Table 1
Geometric properties and experimental results of simulated and tested lattice.

| Analysis Method	Test Type	Unit Cell	Porosity	Cell Size [mm]	Strut Diameter [mm]	Fully Developed f	Fully Developed Nu	Fully Developed Nu, As-Designed Surface Area
LES	Both	BCC	0.75	1.905	0.46	7.1	245	245
LES	Both	Kagome	0.75	2.560	0.80	9.1	240	240
Exp.	Pressure Loss	BCC	–	1.905	0.58	8.6	–	–
Exp.	Pressure Loss	Kagome	–	2.560	0.93	8.7	–	–
Exp.	Heat Transfer	BCC	0.75	1.905	0.41	–	196	231
Exp.	Heat Transfer	Kagome	0.72	2.560	0.86	–	230	269
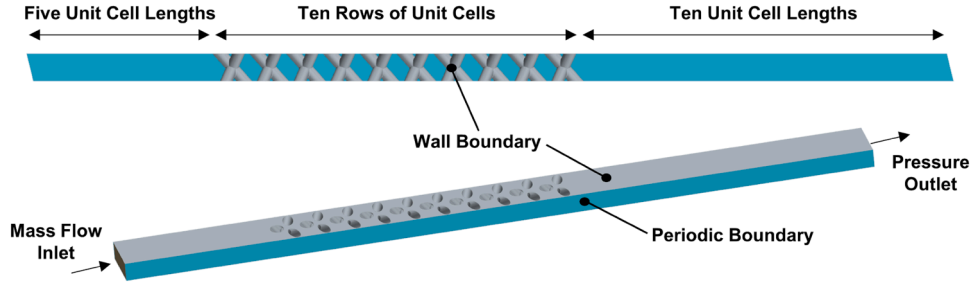
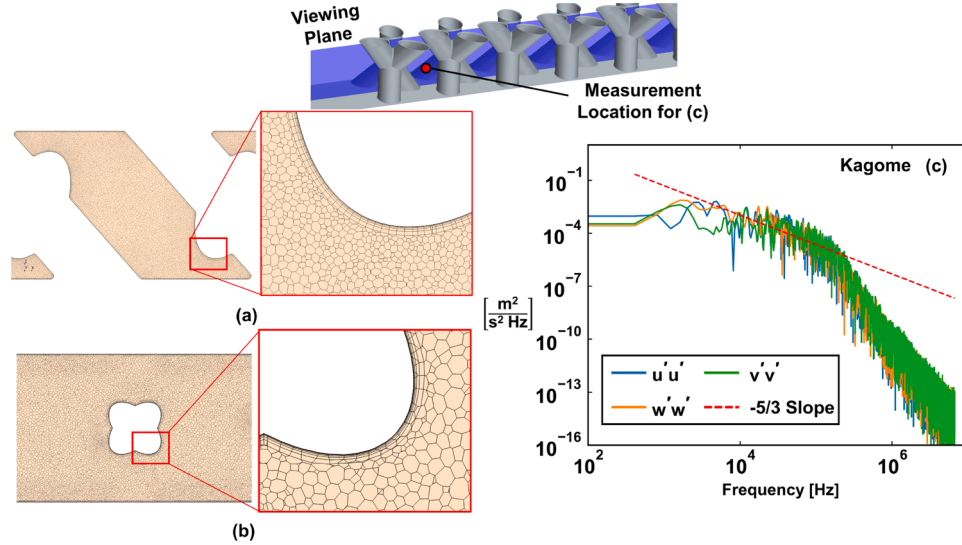**Fig. 2.** Computational domain used for simulations.

Fig. 3. (a) Kagome and (b) body centered cubic mesh at the midplane of the domain and (c) the spectral power density of the three velocity components as a function of frequency at a point downstream of the first row of Kagome lattice.

this analysis as completed for the Kagome lattice is shown in Fig. 3(c), though the BCC lattice had a very similar response. All three components of the velocity from this analysis followed the expected $-5/3$rds slope from a frequency of approximately 10^4 Hz to 10^5 Hz, indicating that the mesh was sufficiently resolved.

After mesh validation was completed, the temperature, pressure, density, and three components of velocity were time averaged at each location in the entire domain for three full residence times in order to capture the bulk fluid motion and thermal transport. A time step was considered converged when all residuals dropped by at least three orders of magnitude. Compute times for both simulations were on the order of several months using 100 cores on a computing cluster. The results of these simulations will be explored in detail in Section 3.

2.3. Benchmarking with experimental simulations

Comparisons of numerically predicted and measured heat transfer and friction factor were made to benchmark the simulations. For the heat transfer experiments, two coupons were manufactured using laser powder bed fusion (L-PBF) on an EOS M280 using Hastelloy-X. A similar sized coupon to those used in prior studies by the authors [30,31] was used to house the lattices. Unlike the modeled domain these coupons contained several more rows of lattice to ensure the flow became fully developed by the coupon exit. Additionally, there were not empty entrance and exit regions in these coupons like in the computational models, and instead the entire interior of the coupons consisted of the lattice core region of the modeled domain. Because of the differences in unit cell size, the manufactured Kagome coupon contained 19 rows of lattice unit cells, and the BCC design contained 25. There were seven

lateral columns of the Kagome lattice in each coupon, and 10 columns in the BCC design. The coupons were CT scanned to validate that they were printed close to the design intent, and a section of the surfaces captured from these scans are is shown in Fig. 4(a) and 4(b). The as-printed porosity was $\varepsilon = 0.72$ for the Kagome lattice and $\varepsilon = 0.75$ for the BCC lattice. It should be noted that because the strut diameter of the BCC lattice was approaching the limits of what could be manufactured on the L-PBF system, there were consequently some variations in the as-printed strut diameter between individual unit cells. This variability and inherent surface roughness resulted in a 17 % increase to surface area for both designs as compared to what was computationally modeled, which was the original design intent.

To compare the predicted and measured pressure losses, two additional coupons were printed on a standard Stereolithography (SLA) 3D
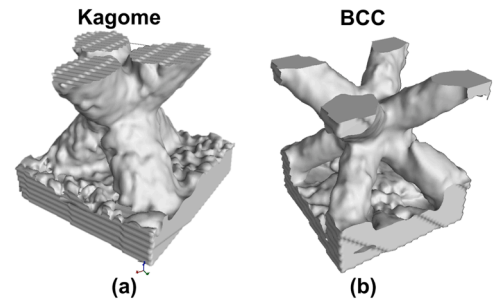

Fig. 4. Single unit cell from CT scan of metal (a) Kagome and (b) BCC lattice test coupons.

printer that represented the computational domain more precisely. These SLA coupons featured the upstream and the downstream regions without lattice that was present in the computational domain. These coupons were also instrumented with pressure taps along the streamwise length to capture local static pressures. Following testing these coupons were cut open and the struts were measured using calipers. Both designs featured struts larger than the design intent, with the diameter of the BCC struts measured to be 0.58 ± 0.06 mm and the Kagome struts were measured to be 0.93 ± 0.06 mm.

Experiments were performed in a benchtop test that has been described in detail in prior publications by the authors [30,31]. In brief, the test rig features an upstream mass flow controller that meters the flow of air through an instrumented test section. This test section features two plenums that condition the flow entering the coupon to be of uniform velocity, and the flow exhausting from the plenum to undergo sudden expansion, ensuring that the inlet and outlet flow conditions were known. Each plenum was instrumented with a pressure tap and a differential pressure transducer was used to capture the static pressure loss across the coupon. The pressure inside of the test section was determined using a gage pressure sensor that measured the downstream static pressure, and the local atmospheric pressure was used to determine the absolute pressure. The plenums in the rig were also instrumented with a series of thermocouples that were used to calculate the temperature of air upstream and downstream of the plenum. Isentropic flow relations were used to determine the temperatures and pressures exactly at the coupon inlet and outlet.

To quantify the internal heat transfer coefficients, a heating assembly was installed on both sides of a test coupon that imposed a constant surface temperature boundary condition. These assemblies consisted of a surface heater placed between insulating foam and a copper block. Six thermocouples were placed precisely halfway through the thickness of the copper block in each heating assembly. Throughout both the foam blocks and the plenums there were a series of thermocouples which were used to determine the conduction losses, which were typically less than 1 %. The temperature from the thermocouples in the copper blocks and the total heater power minus any losses were used in a one-dimensional conduction analysis to determine the coupon surface temperature. An energy balance was also performed during the experiments providing better than 3 % closure.

Both test coupon geometries were tested at the same conditions used in the computational setup. The only deviation for the testing from the computational model was for the SLA coupons used to measure the local pressure loss, which were conducted at room temperature.

2.4. Data reduction

There are many scaling methods used throughout the literature in studying lattice structures specifically related to the performance of their designs. Those variations include a range of geometric features representing the length scales used such as duct hydraulic diameter, largest pore diameter, some combination of surface area and volume, and porosity. Caket et al. [37] have recently assembled a comprehensive summary of studies investigating the performance of lattice structures and noted that due to the unclear length scales it is difficult to directly compare the performance of lattice between studies.

For this study the Reynolds number (*Re*), friction factor (*f*), and Nusselt number (*Nu*) were scaled using the open duct hydraulic diameter. Since the computational results featured an infinitely wide duct due to the periodic boundary conditions, the hydraulic diameter definition reduces to twice the height of the duct, or 2*H*. For the experimental results the test coupon hydraulic diameter was used, though it should be noted that due to the high aspect ratio of the test coupon duct (10:1), the resulting hydraulic diameter was 10 % smaller than that of the infinite duct. For the velocity scale the mass average inlet velocity for a fully open duct was used for both the experimental and the computational domains. As such, the definitions for the Reynolds

number (*Re*), friction factor (*f*), and Nusselt number (*Nu*) are given in Eqs. (1)–(3).

$$Re = \frac{u_{m,in} \cdot \rho_{in} \cdot D_h}{\mu} \tag{1}$$

$$f(x) = \frac{D_h}{\frac{1}{2}\rho u_{m,\ in}^2} \frac{\partial \overline{P}}{\partial x}(x) \tag{2}$$

$$Nu(x) = \frac{h(x) \cdot D_h}{k} \tag{3}$$

The local pressure gradient was found by first taking the average of the streamwise pressure, and then using a third order central differencing scheme to extract the gradient of this pressure as a function of streamwise position. The local heat transfer coefficient was determined using Eq. (4), which was found by combining the equation for internal heat transfer with a constant surface temperature and the first law of thermodynamics.

$$h(x) = \frac{\dot{m} \cdot c_p \cdot (T_m(x) - T_{in})}{A_s(x)} \cdot \frac{\ln\left(\frac{T_{wall} - T_{in}}{T_{wall} - T_m(x)}\right)}{T_{in} - T_m(x)} \tag{4}$$

The surface area at a given streamwise position is defined as the area from the inlet to that position.

Finally the local fluid temperature throughout this study was normalized using Eq. (5).

$$\theta_{x,y,z} = \frac{T(x, y, z) - T_{in}}{T_{wall} - T_{in}} \tag{5}$$

3. Results and discussion

3.1. Local pressure drop and heat transfer

Measurements from the SLA test coupons and predictions of the development of the pressure loss in terms of a friction factor as a function of number of unit cells is shown in Fig. 5(a). The results shown in Fig. 5(a) indicate relatively good agreement between the pressure measurements and predictions, especially for the Kagome geometry. The trend in the results for the BCC agree with the experiments, however, there is a slight overprediction of the friction factor as the flow becomes fully developed. This disagreement is attributed to the sensitivity to the strut diameter for the BCC lattice. As previously discussed, the strut diameter approached the size limit for what could be printed and resulted in slightly larger struts than intended as shown in Table 1. Consequently, the pressure drop from the BCC coupons was measured to be higher than predicted computationally. Both the strut diameters and the unit cell size were larger for the Kagome lattice than they were for the BCC lattice. This meant that even though the SLA Kagome lattice coupons had a similar level of deviation from the intended strut diameter as the BCC lattice, the impact on the overall lattice porosity was smaller, translating to a smaller impact on the expected pressure drop. Given that the Kagome and BCC lattice used similar computational setups and that the experimental measurements from the Kagome lattice had good agreement with the computational results, it was concluded that the simulations represented the internal flow field from the test coupons.

The computational predictions show an oscillatory trend in friction factor beyond the first row for both the BCC and Kagome lattice as shown in Fig. 5(a). These oscillations correlate directly with the flow's interactions with lattice struts. The areas of tightest flow constriction in each of the lattice designs force the flow to accelerate, increasing the pressure loss and consequently increasing the local friction factor. Additionally, the flow stagnates on the lattice struts, which increases the static pressure in front of the lattice followed by a decrease in the static pressure in the wakes that form behind the struts. Because these high-
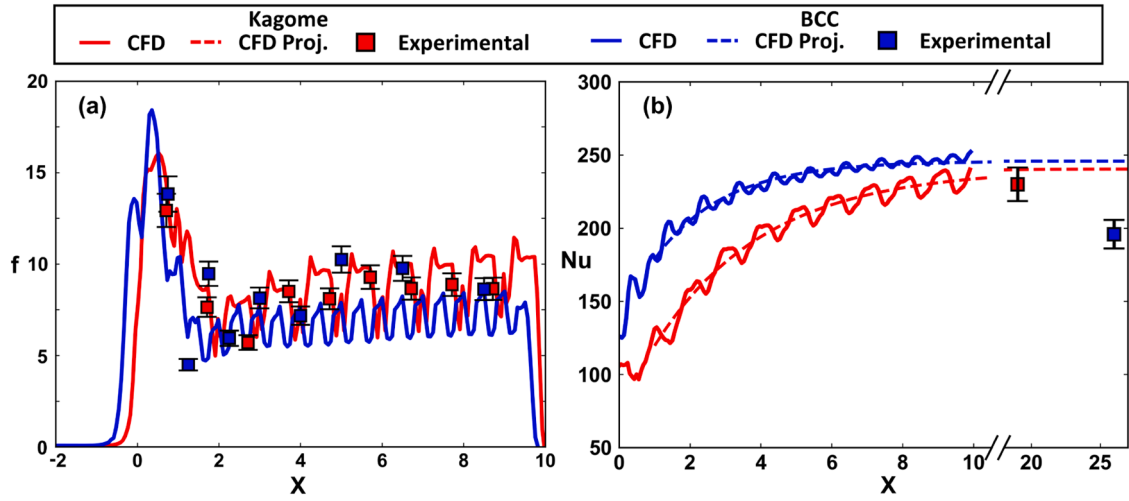
Fig. 5. (a) Friction factor and (b) Nusselt number as a function of X.

and low-pressure regions are a function of the flow's interactions with lattice struts, the increased number of struts in the BCC lattice as compared to the Kagome lattice results in a higher oscillation frequency for the BCC lattice relative to the Kagome. Because the Kagome lattice struts are larger than the BCC lattice, larger wakes with more significant flow area reductions are induced causing the amplitude of Kagome lattice's oscillations to be greater than those seen in the BCC lattice.

For the Kagome lattice, the friction factor oscillates around a constant value after approximately four unit cells, whereas the BCC lattice's friction factor oscillates around a constant value after two unit cells. This near constant oscillation is indicative of the flow becoming hydrodynamically fully developed. Taking the average of friction factor in the region between $X = 5$ and $X = 9$ shows that fully developed value for the Kagome lattice is $f = 9.1$ and the fully developed value for the BCC lattice is $f = 7.1$. For comparison, the friction factor of the Kagome and BCC lattice were found experimentally to be $f = 8.7$ and $f = 8.6$ respectively. The deviation for the BCC lattice is the result of the overbuild struts, as mentioned previously. The Kagome lattice experimental results were within experimental uncertainty of the computational results. This difference in friction factor can be attributed to differences in local wall shear stress and in the strength and distribution of eddies in the wake regions of each lattice, which will be discussed in greater detail in Sections 3.2 and 3.3 respectively.

In addition to the development of the local friction factor profiles, there is significant interest in the development of the local Nusselt number, which is shown in Fig. 5(b). Since the computational domain had fewer unit cells than the experiments with the measured heat transfer values being only a global average, the direct comparisons between the predicted and measured were not possible. However, the predictions in Fig. 5(b) indicate nearly a fully thermally developed BCC lattice while the Kagome appears to continue to increase at the end of the domain. To compare the predicted to the measured Nusselt numbers, shown in Fig. 5(b), a curve fit between row values of $X = 0.5$ and $X = 9.5$ for both lattices were done and are shown using a dashed line. The fully developed projected Nusselt value approaches $Nu = 245$ compared to the measured being $Nu = 196$ for the BCC lattice whereas the projected and measured values for the Kagome lattice were $Nu = 240$ and $Nu = 230$, respectively. The BCC and Kagome lattices reaches 95 % of the projected fully developed value by $X = 4.5$ and $X = 8.3$. This difference in predicted heat transfer is the result of differences to the local thermal profiles, which is discussed in more detail in Sections 3.2 and 3.3.

Comparing the experimental data to the computational data, it is clear that the Kagome lattice LES matches the experimental value within uncertainty, but the BCC design does not. The Nusselt number of these lattice is primarily impacted by two things: the porosity and surface area

of the lattice. The porosity of the experimental BCC lattice was the same as the computational model, whereas the experimental Kagome lattice was slightly less porous due to overbuilding during manufacturing and surface roughness features. Because the experimental Kagome lattice coupons were less porous than computational model, the experimental heat transfer should have been greater than the simulated heat transfer [24], but instead it was slightly lower. Both of the experimental lattice coupons had 17 % greater surface area than intended due to local roughness features present on the surfaces of the struts. If the as-designed surface area was used to calculate the Nusselt number, the fully developed value increases to $Nu = 231$ and $Nu = 269$ for the BCC and Kagome lattice respectively. This adjustment to the surface area makes the BCC lattice performance agree with the computational model within experimental uncertainty, and makes the experimental Kagome lattice have a significantly greater Nusselt number than the computational model, as would be expected due to the decreased porosity. The better agreement using the as-designed surface area implies that the added surface roughness did not effectively increase heat transfer. The fully developed Nusselt number and friction factor for the experimental and computational analysis are summarized in Table 1, using both the as-printed and as-designed surface areas.

Similar to the momentum development there is a distinct spatial periodicity in the Nusselt number of the Kagome lattice, oscillating as the flow navigates around each row of lattice. This periodicity reaches a minimum at the center of a Kagome unit cell, indicating the sudden flow area reduction results in a local decrease to the Nusselt number. The BCC lattice's Nusselt number was notably less periodic by comparison, with a somewhat uniform increase in Nusselt number as a function of number of unit cells. The variation in oscillations between the two lattices is a function of local velocity and thermal profiles, which will be discussed later in Section 3.2.

3.2. Flow and thermal developing region

To better understand how the flow develops through the entry region of the lattice structures, normalized, time-averaged thermal and velocity profiles at five streamwise planes were taken normal to the flow. The profiles for the Kagome lattice are shown in Fig. 6. Starting with the Kagome lattice shown in Fig. 6(a-j), the predictions indicate significant secondary flows including flow reversals that result in thermal fields with large variations. The secondary velocities for the Kagome lattice take the form of a vortex pair that drives the flow to have the highest velocities near the bottom juncture with the adjacent cell. Between the 1st (Fig. 6(b)) and 2nd (Fig. 6(c)), rows of lattice there are also smaller, weaker vortices present in the bottom corners of the Kagome lattice,
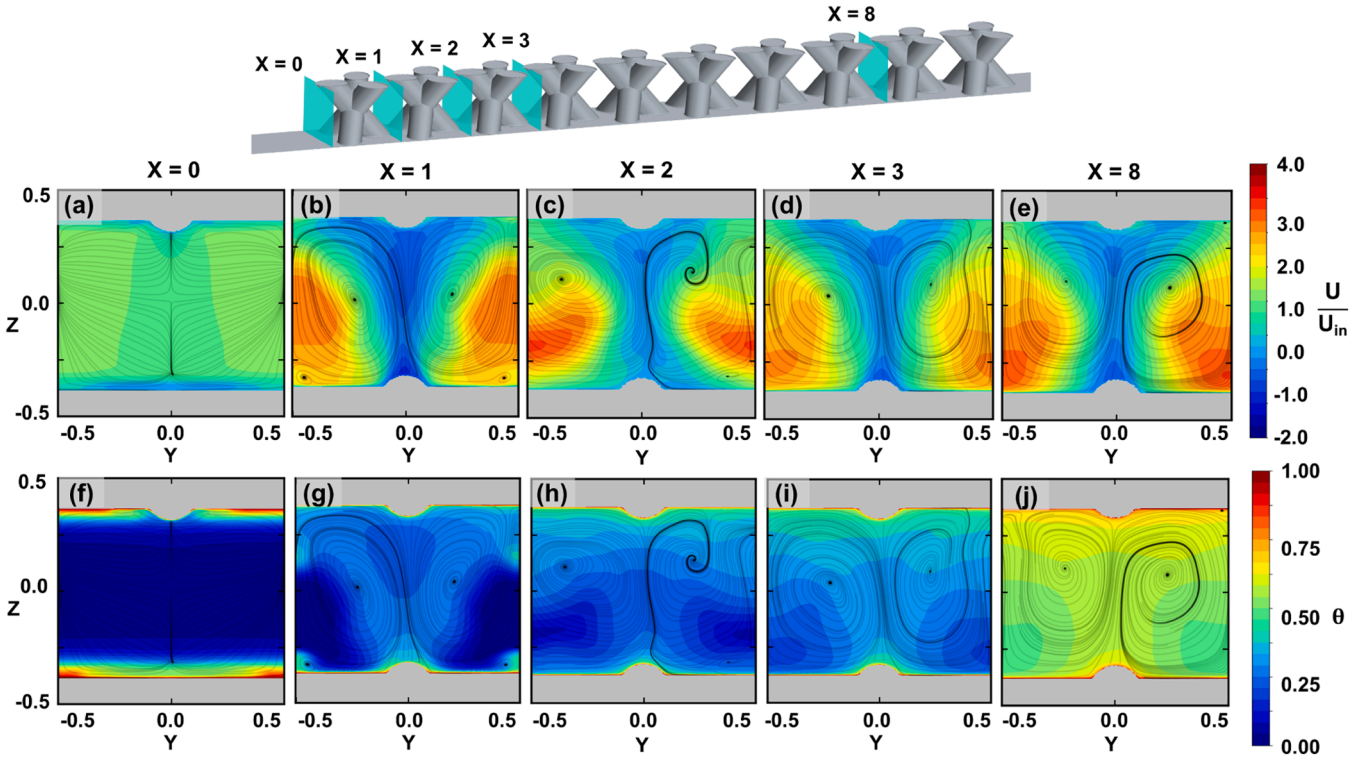
Fig. 6. Normalized time-averaged (a-e) velocity and (f-j) thermal contours at five streamwise planes for the Kagome lattice.

which dissipate after the 3rd (Fig. 6(d)) row of lattice. These smaller vortices are the result of the upstream horseshoe vortex which forms just in front of the first row of the Kagome lattice. In the later rows of the Kagome lattice, the time-averaged horseshoe vortices are not visible resulting from the unsteady shedding from the struts. The thermal profiles for the Kagome lattice, shown in Fig. 6(f-j), result explicitly from the secondary velocities with the cooler air near the bottom of the channel convecting towards the top of the channel.

The velocity distribution presented in Fig. 6(c) indicates that after the second unit cell the flow accelerates as it transitions to fully developed from the distribution shown in Fig. 6(b) and Fig. 6(d). During this transition, there is a significant increase in turbulence intensity, which will be discussed in Section 3.3. The bulk of the flow can be seen to be moving on either side of the wake of the lattice in the first row (Fig. 6(b)) with the secondary flows appearing to be similar between the third (Fig. 6(d)) and eighth rows(Fig. 6(e)). This similarity between the 3rd and the 8th rows of lattice is represented in the friction factor shown in Fig. 5(a), where after the third row the trend in friction factor becomes spatially periodic. For the fully developed flow, there are regions of high velocity near the base of both sides of the lattice unit cell as
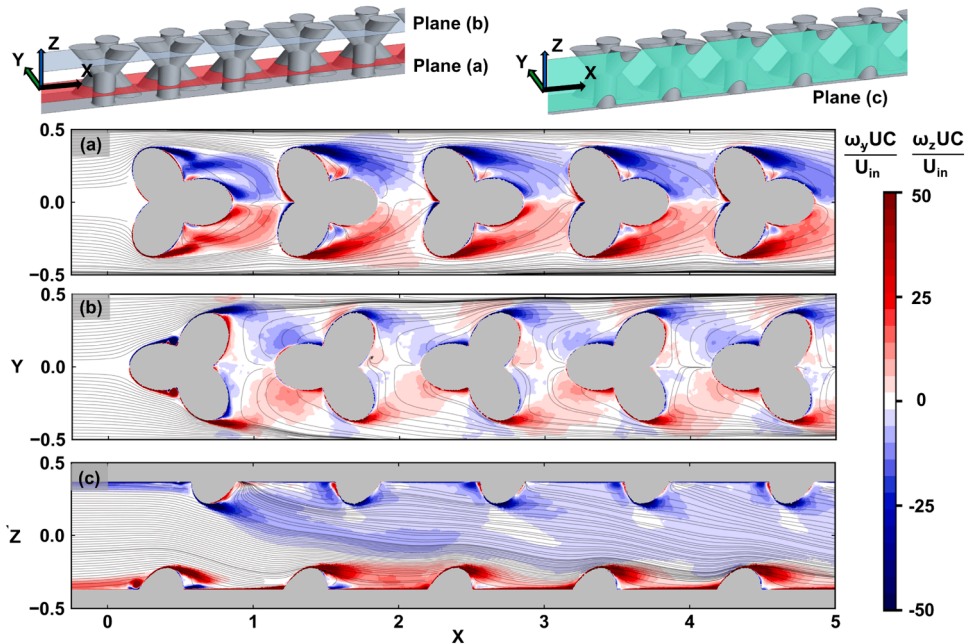

Fig. 7. Normalized time-averaged vorticity in three streamwise planes for the first five rows of the Kagome lattice (a-c).

shown in Fig. 6(d). The biased flow resulted in 15 % greater heat transfer on the base of the channel than on the top surface, similar to what was reported previously by Liang et al. [8]. To explore this formation in greater detail, contours of the time-averaged normalized vorticity with in-plane streamlines are shown for three streamwise planes in Fig. 7.

As the flow encounters the first Kagome unit cell, it impinges on the two front facing struts in the base of lattice and the one front facing strut at the top of the lattice. While the flow navigates around the base of the lattice, a region of vortical flow can be seen in Fig. 7(a) on either side of the first unit cell, showing the formation of a wake. Some amount of the flow that encounters this first row passes between the bottom two struts and is injected into this wake, forming another vortex pair that extends to the following unit cell. The flow that is captured in these wakes is directed into the backwards facing strut near the base of the channel. This strut forces the fluid in the center of the unit cell upwards. Along the top of the channel the flow is diverted to either side of the unit cell by the single front facing lattice strut, and then collides with and subsequently separates from the two back facing struts as seen in Fig. 7(b). As the wake forms from these separation points it is interrupted by the front facing strut from the second lattice unit cell. This interruption forces the flow and wake downwards, as shown by the streamlines in Fig. 7(c). The composite effect between the interior flow being directed upwards and the exterior flow near the periodic boundaries being directed downwards results in the rotational secondary flows between cells that were seen previously in Fig. 6.

Continuing downstream, the flow along the base of the channel passes over the front facing struts of the second row of lattice, and a larger wake forms that occupies the full width between the second and third unit cells. Because the top surface wake from the first unit cell is also continuing downstream, the flow area becomes effectively reduced and results in the high velocity region that was identified in Fig. 6(c). Beyond the third lattice unit cell, the wake from the top struts of the first unit cell diffuses as the flow becomes highly mixed. This reduces the maximum flow speeds, however the rotational flow between cells continues to drive the fluid near the periodic boundaries downwards, and

the flow in the interior upwards, as was seen in Fig. 6.

The Kagome lattice flow fields are significantly different from the BCC lattice's, as shown in Fig. 8 (a-e). There are many more vortices present for the BCC lattice than for the Kagome, with each BCC strut generating a pair of vortices. The generation of these vortices leads to periodic performance in friction factor seen in Fig. 5(a), and the vortices smaller size relative to the Kagome vortices result in less pressure drop. The BCC vortices increase mixing from the near wall region, distributing flow from the center of the channel with higher velocities at the junction between the cells and in the near wall regions. After three unit cells ($X = 3$), the velocity distribution shows the highest velocities occurring between the cell junctures. These high velocity regions transport the upstream cooler fluid downstream as shown in the thermal fields in Fig. 8 (j). Increased mixing from the secondary flows in the wakes of the BCC lattice resulted in higher Nusselt numbers as compared to the Kagome lattice, as was seen in Fig. 5(b).

Just after the first row of lattice (Fig. 8(b)), the flow is largely distributed to the regions near the center of the periodic boundary at $Y = -0.5$ and $Y = 0.5$ and along center of the top and bottom walls at $Z = -0.4$ and $Z = 0.4$. After the second row ($X = 2$), there is a notable bias of the flow to the cell junctures as shown in Fig. 8(d), as the bottom and top walls induce increased drag reducing the overall flow through these regions. The flow distribution at these planar locations remains largely the same after the second row. Unlike the flow distributions seen with the Kagome lattice, there is a distinct symmetry to the flow distributions present for the BCC lattice, stemming from the overall symmetry of the geometry.

The time-averaged streamwise thermal and velocity fields at a vertical and horizontal midplane section for the Kagome and BCC lattice are shown in Figs. 9 and 10, including zoomed in regions after the 1st and 8th cells. Along the base of the channel in the core region of both lattice the thermal boundary layer is very thin relative to the developed boundary layer just upstream of the lattice at $X = 0$ due to the locally increased flow speeds, as shown in Figs. 9(b) and 10(b). These thin boundary layers enhance heat transfer significantly by enabling a higher
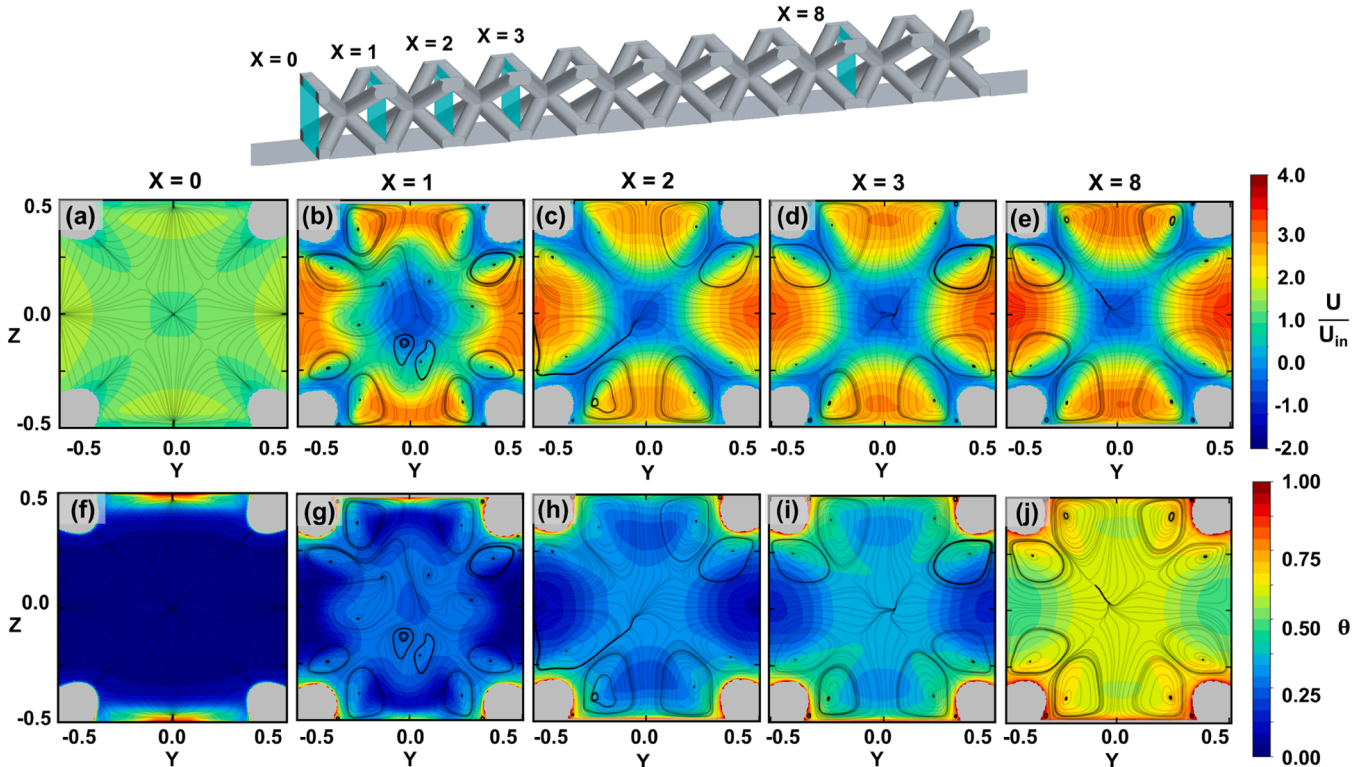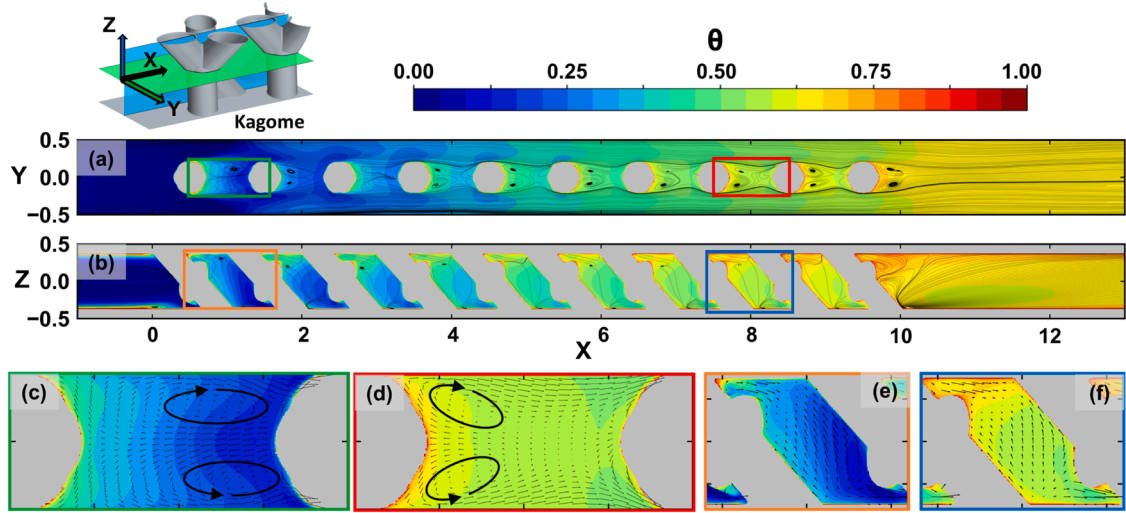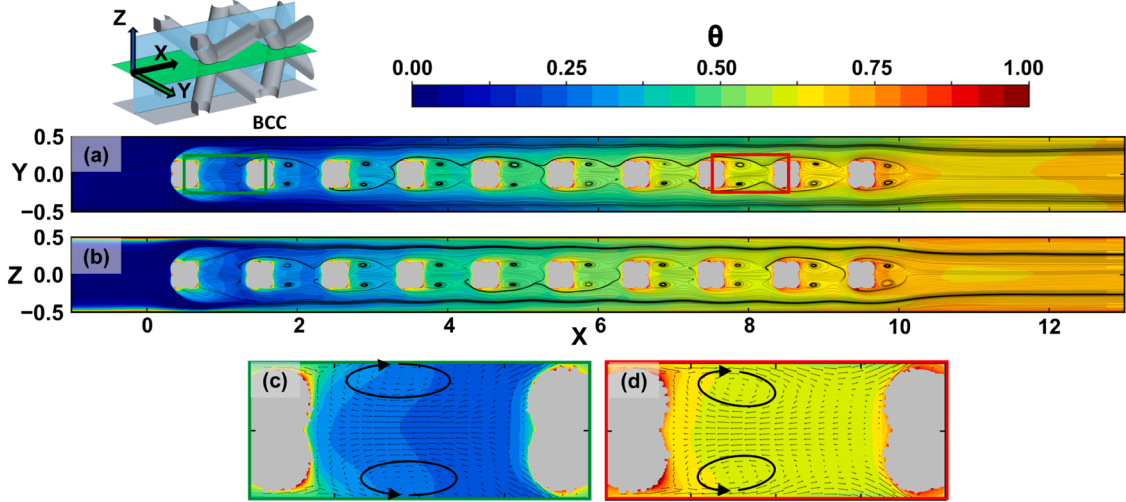

Fig. 8. Normalized time-averaged (a-e) velocity and (f-j) thermal contours at five streamwise planes for the BCC lattice.

Fig. 9. Normalized time-averaged thermal contours with streamlines in the (a) horizontal and (b) vertical midplane of the Kagome lattice with highlighted regions of interest (c-f).

Fig. 10. Normalized time-averaged thermal contours with streamlines in the (a) horizontal and (b) vertical midplane of the BCC lattice with highlighted regions of interest (c,d).

thermal gradient near the wall. In addition to short thermal boundary layers, the heat transfer is also enhanced by the boundary layer detachment in the wake region of the lattice, and the subsequent turbulent mixing which will be explored in Section 3.3. These wakes result in recirculation zones just behind the center of the unit cells, which are shown in Figs. 9(c-d) and 10(c-d) which further enhance mixing and heat transfer. The velocity in these recirculation zones is much slower than those near the periodic boundary, with the flow in some regions being nearly stagnant. In these regions the fluid is able to heat up significantly, such as near the top the of the Kagome lattice as shown in Fig. 9(e-f). However, in the region between two rows of lattice, cooler fluid is transported into this wake by the cooler fluid that was identified in Figs. 6 and 8. This transport results in a decrease in local fluid temperature downstream of the wake, and an example of this phenomenon can be seen in Figs. 9(c) and 10(c). This streamwise thermal gradient is significantly steeper for the Kagome lattice than the BCC lattice due to the increased mixing in the BCC lattice from the secondary flows identified in Fig. 8. The difference in thermal gradient between the two lattice causes the local Nusselt number of the Kagome lattice to have greater peak-to-peak variation than the BCC lattice, as seen in Fig. 5(b).

The streamlines in the horizontal planes displayed in Figs. 9(a) and

10(a) show that the wake behind the first row of both lattice types is notably larger than the downstream wakes. These wakes result in an effective reduction in flow area for this first row, which in tandem with the flow impinging on the first unit cell surface lead to the substantial pressure drop and friction factor presented in Fig. 5(a). The wakes between the second ($X = 3$) and ninth ($X = 8$) rows are similar for both lattice, showing again that the flow has transitioned to being fully developed. A pair of vortices form in the wake region of behind each row of the Kagome and BCC lattices and are indicated using two ovals in Figs. 9(c-d) and 10(c-d). The location of the vortices relative to the center of the BCC unit cell is very similar for all rows of the BCC lattice, but change for the Kagome lattice after the second row. The center of the vortices in the wake of the first row ($X = 1$) are located approximately 0.6 unit cells away from the center of the first row. In all subsequent rows, the center of the wake vortices shifts to be approximately 0.3 unit cells away from the center of the unit cell.

For the BCC unit cell, the vortical formations are the same in both the vertical (Fig. 10(a)) and horizontal (Fig. 10(b)) planes due to symmetry. In contrast, the flow field in the horizontal (Fig. 9(a)) and vertical (Fig. 9 (b)) planes of the Kagome lattice are distinct. Looking to Fig. 9(e-f), the flow in the vertical plane can be seen to move through the bottom struts

of the lattice, and then move upwards towards the top of the channel, following the streamlines that were shown in Fig. 7. Unlike the flow in the horizontal plane, the secondary flows in the vertical plane of the core region were not significantly a function of the streamwise location for the Kagome lattice.

The flow in the wake behind the core region for both lattice designs return to the flow distribution found between parallel flat plates after several additional rows of lattice. The flow downstream of the BCC lattice shows a fully developed internal flow distribution approximately two unit cells after the core region, but the Kagome lattice takes as many as five unit cell lengths. The fully developed distance downstream of the lattice cells is a function of the Kagome lattice having highly skewed flow along the base of the channel, as was seen in Fig. 6, which continues well after it leaves the core region, as shown using streamlines in Fig. 9 (b) after $X = 10$.

3.3. Turbulence and unsteady flows

The turbulence intensity contours for the two lattices are shown in Fig. 11(a-d) for two different streamwise planes. In general, the turbulence intensity levels are much higher for the Kagome than for the BCC lattices. The Kagome lattice shown in Fig. 11(b) has a peak in turbulence intensity just after $X = 2$ of $TI = 1.61$. The maximum of TI for the Kagome lattice is located where the velocity profiles in the Kagome lattice are not yet fully developed as was seen in Fig. 6, with the high turbulence intensities indicating high flow unsteadiness. The BCC lattice has lower turbulence intensities, shown in Fig. 11(c) and 11(d), with a maximum turbulence intensity of $TI = 0.87$. Regions of high turbulence intensity for both types of unit cell relate to regions of increased heat transfer. Highly rotational regions like those in the wake of a given unit cell experience increased turbulence intensity resulting from the unsteady flow due to the wakes shedding from the struts. The increased turbulence intensity for the Kagome lattice as compared to the BCC lattice is reflected in the friction factor results presented in Fig. 5(a), as the higher turbulence intensity leads to increased pressure drop and subsequently higher friction factor. While generally speaking increases to turbulence intensity results in increases to heat transfer, prior researchers have identified that there is a limit to how much enhancement increased turbulence intensity can provide [38]. This limit is reflected in the heat transfer results, where despite the Kagome lattice having a greater overall turbulence intensity, it has a lower Nusselt number than the BCC lattice.

To identify unsteady flow structures present in these areas of high turbulence intensity, the unsteady y-component of vorticity and

temperature were captured at distinct time intervals for the Kagome and BCC lattice and is shown in Figs. 12 and 13. Beginning with the Kagome lattice in Fig. 12(a), there are many instantaneous vortices in the regions between the first three rows of unit cells in Fig. 12(a). These vortices indicate the flow is highly mixed, especially in the regions of highest turbulence intensity as shown in Fig. 11(b). There does not appear to be any coherent or consistent structures, but instead this flow appears to be dominated by turbulent mixing. Regions of high vortex strength directly correlate with regions of increased thermal transport, as seen in instantaneous theta contours shown in Fig. 12(b). Particularly the vortices that form due to wake shedding, such as those at approximately $Z = 0$, $X = 0.8$, there is substantial thermal transport from the near wall region to the bulk flow. In certain areas of the flow, such as near the top wall at $X = 2$, there is a recirculation zone that limits local heat transfer, denoted by the local vortical flows and temperatures approaching $\Theta = 0.5$.

Just upstream of the Kagome lattice a horseshoe vortex forms along the bottom wall periodically in time and is ingested into the core region of the lattice. This vortex forms, grows in strength, detaches from the wall, and is ingested 16 times per flow through time of the domain. This vortex formation and destruction can be seen at $X = 0.1$ in Fig. 11(b), where there is a slight increase in turbulence intensity, and in the time averaged thermal profiles shown Fig. 9(b), where the boundary layer just upstream of the first row of lattice dissipates before coming into contact with the actual unit cells.

The flow between rows of the BCC lattice has more coherent vortical structures than the Kagome lattice, as shown in Fig. 13(a). At the interface of the upstream flow and the wake of the first row of BCC lattice there is a region of vorticity that is constant in time, indicating flow separation. The separated flow region enables significant thermal transport, as shown in Fig. 13(b). Following the first row, the span of the wake that forms from the center of the unit cell is only the width of the center region, and much of the flow around the lattice is mixed. The mixing in these rows enhances the thermal uniformity of the fluid through the BCC lattice. As these vortices shed from the center of the BCC unit cell, they interact with the boundary layer forming on the endwall, pulling it away from the near wall region. This vortex-boundary layer interaction causes the size of the thermal boundary layer to vary substantially as the fluid passes through the core region and indicates that the fluid near the endwall is circulated into the bulk flow more effectively than was seen for the Kagome lattice. The result of this more substantial interaction is a more uniform increase in the thermal profile than was seen in the Kagome lattice when time averaged, as was shown in Figs. 9 and 10. Subsequently, the local BCC lattice Nusselt
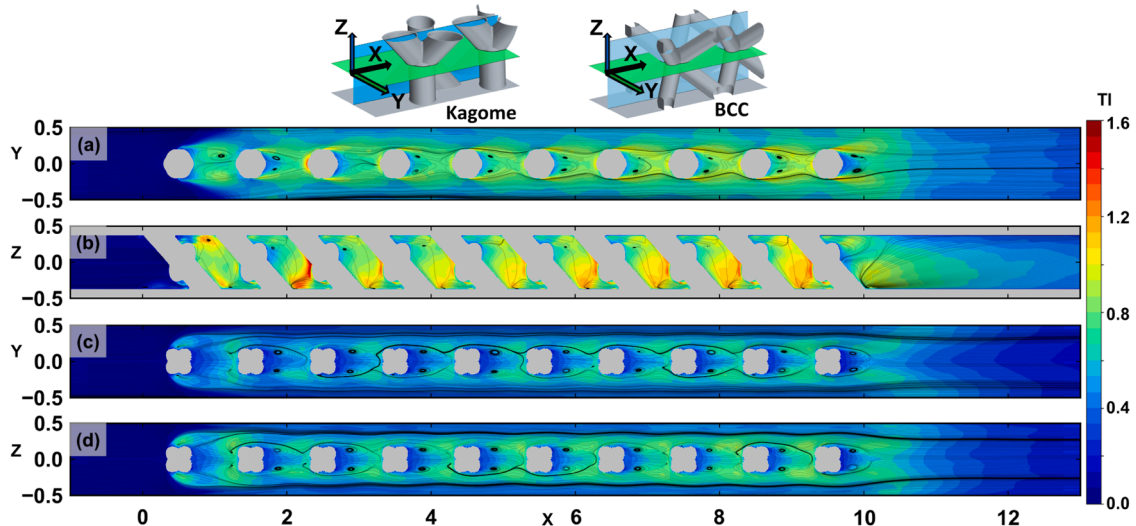

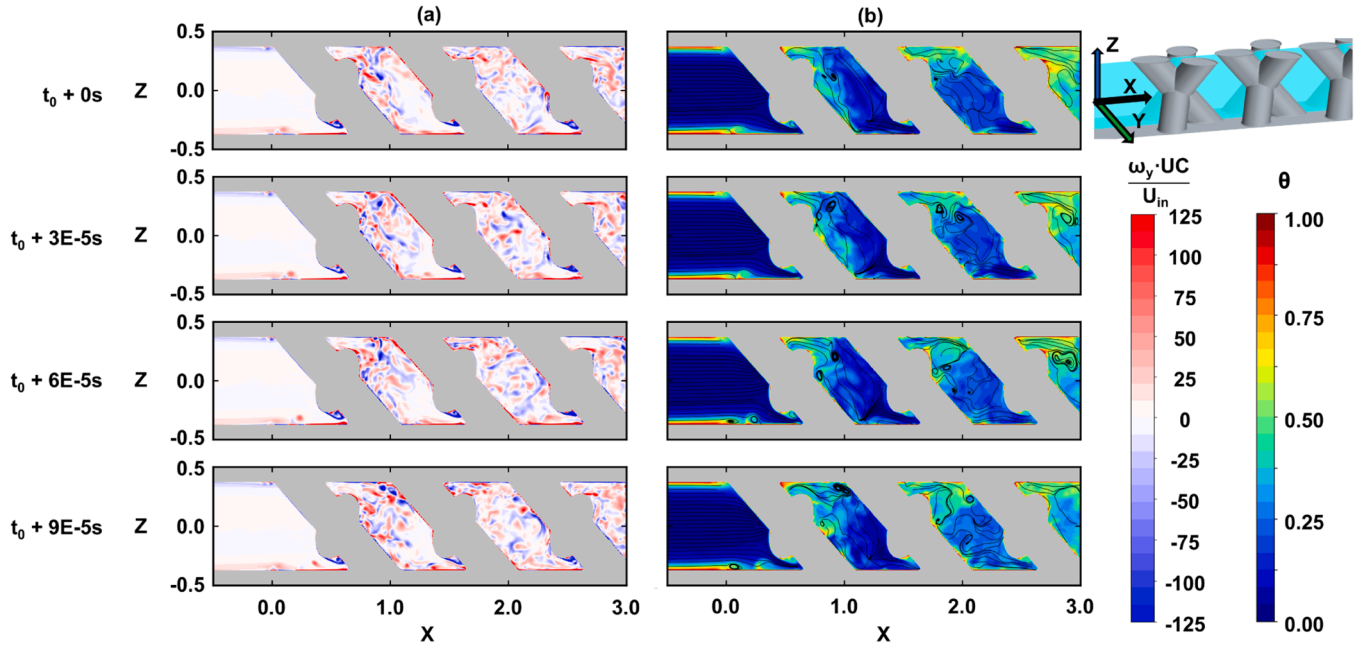**Fig. 11.** Turbulence intensity at two planar locations for the (a-b) Kagome and (c-d) BCC lattice.

Fig. 12. Instantaneous (a) vortices and (b) thermal profiles around the Kagome lattice at four time intervals.
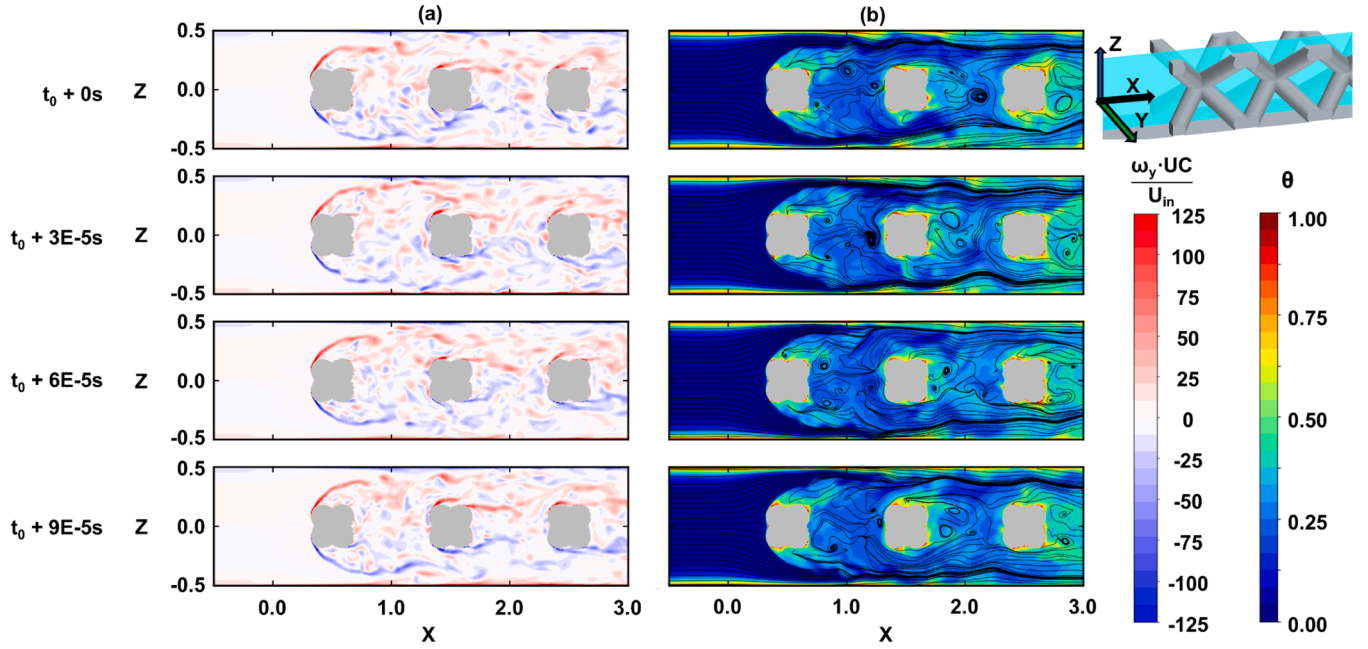

Fig. 13. Instantaneous (a) vortices and (b) thermal profile around the BCC lattice at four time intervals.

number had smaller amplitude oscillations than the Kagome lattice, and the magnitude of the Nusselt number was also greater as shown in Fig. 5 (a).

To understand the fundamental motions of the vortices being shed from the two types of lattices, a transient spectral analysis was completed to determine the dominant frequencies in the U component of velocity. This analysis was completed by saving the instantaneous velocities at every location in the planes shown in Fig. 9(a) and 9(c). The time histories of these velocities were reconstructed, and a fast Fourier transform (FFT) was completed at each point to covert the velocity into the frequency domain. The power spectrum was calculated from the FFT to identify which frequency dominated the local velocity signal. The magnitude of the power spectra of these locally dominant frequencies

varied considerably depending on the location in the spatial domain. To identify the regions of the most significant periodic flow, the frequencies whose magnitude were in the top 25 % of all of the locally dominant frequencies were isolated. To normalize the isolated dominant frequencies (n), the local Strouhal number was calculated and is shown in Fig. 14. The length scale for the Strouhal number was the width of the maximum flow obstruction at the center plane, and the velocity scaling was the local time-averaged velocity.

The Strouhal number is defined as the ratio of unsteady acceleration to the advective acceleration for a flow. For a single bluff body in cross flow, the expected Strouhal number is $St = 0.2$ in flows with a Reynolds number between $Re = 1000$ and $Re = 100,000$ [39]. However, prior investigations have identified that augmentations to the yaw of the
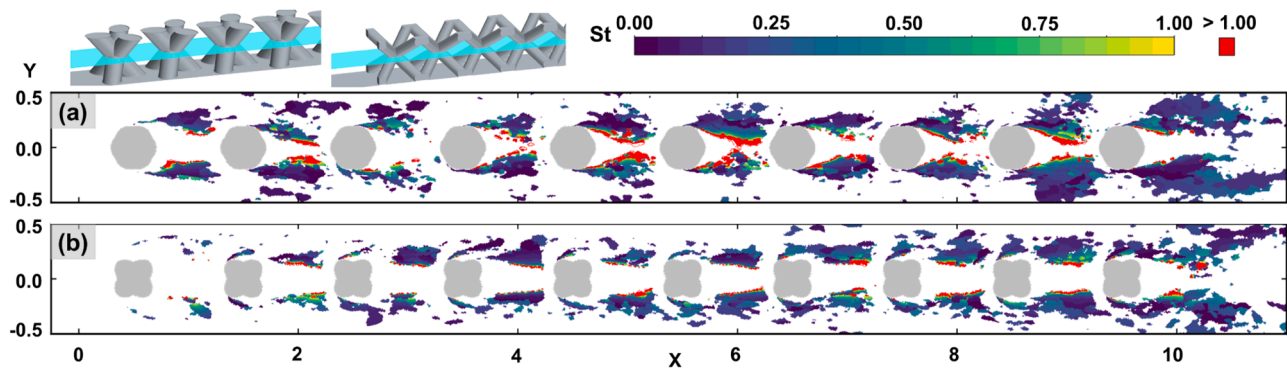
Fig. 14. Local Strouhal number in the wake region of the (a) Kagome and (b) BCC lattice.

cylinder can decrease the Strouhal number [40], and that cylinders in a bank arrangement, such as pin fins, can cause the Strouhal number to increase beyond values of $St = 0.4$ using velocity scaling similar to what was used in this analysis [41].

For the present investigation the regions where the wake shedding occurs is clear, with wakes shedding halfway along the streamwise span of the center of a Kagome lattice unit cell (Fig. 14(a)) and almost immediately after coming into contact with the center of the BCC lattice unit cell. Both locations represent areas where the span of the geometry decreases, which results in a boundary layer separation. The Strouhal numbers associated with these regions near the point of separation and just downstream of it lie in the range of $St = 0.05$ to $St = 0.5$, which is similar to what has been seen in prior pin bank experiments [41], due to large scale alternating eddy shedding [42]. The local Strouhal number increases to well in excess of $St = 1.0$ at the wake interface just behind the center of a given lattice unit cell due to high frequency vortices present in the wake region, as was seen in Figs. 12 and 13. In these regions the high frequency vortices that form in the shear layer of the wake dominates local oscillations in the flow and the associated Strouhal number, as compared to lower frequency instabilities due to the alternating eddy shedding. In the wake of the final row of lattice, the regions of the flow where $St > 1.0$ for both the BCC and Kagome designs are less prominent, but there are larger regions of more moderate Strouhal numbers ($St = 0.05$–0.4). In these regions the alternating eddies from the final row of lattice propagate downstream and are not interrupted by additional rows of lattice, allowing the vortices shed in this region extend out to full span, unlike what was seen in the earlier rows. For the Kagome lattice shown in Fig. 14(a), the regions of the flow outlined by Strouhal numbers greater than one are cylindrical in all but the regions behind the first and last row, whereas these regions are largely rectangular in shape for the BCC lattice shown in Fig. 14(b). In the regions of the flow where $St > 1.0$, the time averaged local velocities approach 0 as the flow transitioned to being reversed in the wake of the lattice, as was seen in Figs. 9 and 10. As was seen in Figs. 12 and 13, the local flow instabilities characterized by the Strouhal number enhanced thermal transport, which subsequently increased the local Nusselt number. These periodic flow mechanisms also increased viscous dissipation, resulting in significant pressure losses and friction factor values.

4. Conclusion

Two lattice structure designs were explored using large eddy simulations to understand underlying physical phenomena regarding thermal and momentum development, as well as unsteady flow features that result in high turbulence regions. Simulations were compared to experimental results and showed generally good agreement, and reasons for deviations between the two methods were identified. The friction factor for Kagome and BCC lattice was seen to become fully developed after four and two unit cells respectively, with the Kagome lattice friction factor being greater than the BCC lattice friction factor. The number

of unit cells before the flow became fully developed was found to be a function of the local velocity distribution. The flow thermally developed within approximately four unit cells for the BCC designs and after eight unit cells for the Kagome, which was found to be the result of variations in the velocity profile and changes to the secondary flow structures as the fluid moved downstream. Once fully developed, the flow in the Kagome lattice was skewed, with one side of channel featuring two high velocity regions. The two high velocity regions were found to develop due to the interactions between the rotational wake regions and the lattice struts. The turbulence intensity was found to be a function of lattice unit cell design, with the Kagome lattice having higher local turbulence intensity than the BCC design. This variation was found to be the result of highly unsteady flow that formed as the Kagome lattice approached a fully developed flow condition. Vortices shed from both the BCC and Kagome lattice interacted with the endwalls, resulting in periodic boundary layer detachment in the wake region of the lattice designs, which ultimately enhanced heat transfer. Spectral analysis revealed that the wake shedding in the core lattice region occurred at a similar Strouhal numbers to prior pin bank experiments, with some regions of periodic flow dominated by large scale alternate eddies and other regions dominated by vortices present in the wake shear layer.

This study uniquely identified the time dependent structures present in the Kagome and BCC lattice designs, and further classified the development of friction factor and Nusselt number through rows of these lattice. The specific flow structures that contributed to this development were also determined and described in detail. This study also highlighted the use of large eddy simulations as a viable and valuable method for exploring lattice structure performance. Future work will be needed to explore additional styles of lattice structures, and identify how best to scale their performance to enable use in a myriad of applications.

Author statement

The following list the contribution of each author to the development of the manuscript, Thomas Corbett: Development, Simulation, Data curation, Analysis, Figures, Writing – original draft, review, & editing. Karen Thole: Development, Writing – review & editing

CRediT authorship contribution statement

Thomas M. Corbett: Data curation, Formal analysis, Writing – original draft, Writing – review & editing. **Karen A. Thole:** Writing – review & editing.

Declaration of Competing Interest

Data availability

Data will be made available on request.

Acknowledgements

References

[1] I. Kaur, Y. Aider, K. Nithyanandam, P. Singh, Thermal-hydraulic performance of additively manufactured lattices for gas turbine blade trailing edge cooling, Appl. Therm. Eng. 211 (2022) 118461, https://doi.org/10.1016/j.applthermaleng.2022.118461.

[2] B. Shen, Y. Li, H. Yan, S.K.S. Boetcher, G. Xie, Heat transfer enhancement of wedge-shaped channels by replacing pin fins with Kagome lattice structures, Int. J. Heat Mass Transf. 141 (2019) 88–101, https://doi.org/10.1016/j.ijheatmasstransfer.2019.06.059.

[3] J.Y. Ho, K.C. Leong, T.N. Wong, Additively-manufactured metallic porous lattice heat exchangers for air-side heat transfer enhancement, Int. J. Heat Mass Transf. 150 (2020), 119262, https://doi.org/10.1016/j.ijheatmasstransfer.2019.119262.

[4] I. Kaur, P. Singh, Critical evaluation of additively manufactured metal lattices for viability in advanced heat exchangers, Int. J. Heat Mass Transf. 168 (2021), 120858, https://doi.org/10.1016/j.ijheatmasstransfer.2020.120858.

[5] I. Kaur, P. Singh, Flow and thermal transport characteristics of Triply-Periodic Minimal Surface (TPMS)-based gyroid and Schwarz-P cellular materials, Numer. Heat Transf. Part Appl. 79 (2021) 553–569, https://doi.org/10.1080/10407782.2021.1872260.

[6] Z. Cheng, R. Xu, P.X. Jiang, Morphology, flow and heat transfer in triply periodic minimal surface based porous structures, Int. J. Heat Mass Transf. 170 (2021), 120902, https://doi.org/10.1016/j.ijheatmasstransfer.2021.120902.

[7] D.A. Clarke, F. Dolamore, C.J. Fee, P. Galvosas, D.J. Holland, Investigation of flow through triply periodic minimal surface-structured porous media using MRI and CFD, Chem. Eng. Sci. 231 (2021), 116264, https://doi.org/10.1016/j.ces.2020.116264.

[8] D. Liang, G. He, W. Chen, Y. Chen, M.K. Chyu, Fluid flow and heat transfer performance for micro-lattice structures fabricated by Selective Laser Melting, Int. J. Therm. Sci. 172 (2022), 107312, https://doi.org/10.1016/j.ijthermalsci.2021.107312.

[9] D. Liang, C. Shi, W. Li, W. Chen, M.K. Chyu, Design, flow characteristics and performance evaluation of bioinspired heat exchangers based on triply periodic minimal surfaces, Int. J. Heat Mass Transf. 201 (2023), 123620, https://doi.org/10.1016/j.ijheatmasstransfer.2022.123620.

[10] T. Kim, H.P. Hodson, T.J. Lu, Fluid-flow and endwall heat-transfer characteristics of an ultralight lattice-frame material, Int. J. Heat Mass Transf. 47 (2004) 1129–1140, https://doi.org/10.1016/j.ijheatmasstransfer.2003.10.012.

[11] S. Parbat, Z. Min, L. Yang, M. Chyu, Experimental and Numerical Analysis of Additively Manufactured Inconel 718 Coupons With Lattice Structure, J. Turbomach. 142 (2020), 061004, https://doi.org/10.1115/1.4046527.

[12] D. Liang, W. Bai, W. Chen, M.K. Chyu, Investigating the effect of element shape of the face-centered cubic lattice structure on the flow and endwall heat transfer characteristics in a rectangular channel, Int. J. Heat Mass Transf. 153 (2020), 119579, https://doi.org/10.1016/j.ijheatmasstransfer.2020.119579.

[13] L. Xu, H. Chen, L. Xi, Y. Xiong, J. Gao, Y. Li, Flow and heat transfer characteristics of a staggered array of Kagome lattice structures in rectangular channels, Heat Mass Transf 58 (2022) 41–64, https://doi.org/10.1007/s00231-021-03100-2.

[14] D. Liang, W. Chen, Y. Ju, M.K. Chyu, Comparing endwall heat transfer among staggered pin fin, Kagome and body centered cubic arrays, Appl. Therm. Eng. 185 (2021), 116306, https://doi.org/10.1016/j.applthermaleng.2020.116306.

[15] I. Kaur, P. Singh, Numerical investigation on conjugate heat transfer in octet-shape-based single unit cell thick metal foam, Int. Commun. Heat Mass Transf. 121 (2021), 105090, https://doi.org/10.1016/j.icheatmasstransfer.2020.105090.

[16] I. Kaur, Flow and Thermal Transport in Additively Manufactured Metal Lattices Based On Novel Unit-Cell Topologies, MIssissippi State University, 2022. scholarsjunction.msstate.edu/td/5587/.

[17] I. Kaur, P. Singh, Conjugate heat transfer in lattice frame materials based on novel unit cell topologies, Numer. Heat Transf. Part Appl. (2022) 1–14, https://doi.org/10.1080/10407782.2022.2083874.

[18] I. Kaur, P. Singh, Direct Pore-Scale Simulations of Fully Periodic Unit Cells of Different Regular Lattices, J. Heat Transf. 144 (2022), 022702, https://doi.org/10.1115/1.4053204.

[19] I. Kaur, P. Singh, Flow and Thermal Transport Through Unit Cell Topologies of Cubic and Octahedron Families, Int. J. Heat Mass Transf. 158 (2020), 119784, https://doi.org/10.1016/j.ijheatmasstransfer.2020.119784.

[20] Y. Aider, I. Kaur, H. Cho, P. Singh, Periodic heat transfer characteristics of additively manufactured lattices, Int. J. Heat Mass Transf. 189 (2022), 122692, https://doi.org/10.1016/j.ijheatmasstransfer.2022.122692.

[21] G. Yang, C. Hou, M. Zhao, W. Mao, Comparison of convective heat transfer for Kagome and tetrahedral truss-cored lattice sandwich panels, Sci. Rep. 9 (2019) 3731, https://doi.org/10.1038/s41598-019-39704-2.

[22] B. Shen, H. Yan, H. Xue, G. Xie, The effects of geometrical topology on fluid flow and thermal performance in Kagome cored sandwich panels, Appl. Therm. Eng. 142 (2018) 79–88, https://doi.org/10.1016/j.applthermaleng.2018.06.080.

[23] U. Kemerli, K. Kahveci, Conjugate forced convective heat transfer in a sandwich panel with a Kagome truss core: the effects of strut length and diameter, Appl. Therm. Eng. 167 (2020), 114794, https://doi.org/10.1016/j.applthermaleng.2019.114794.

[24] T. Dixit, P. Nithiarasu, S. Kumar, Numerical evaluation of additively manufactured lattice architectures for heat sink applications, Int. J. Therm. Sci. 159 (2021), 106607, https://doi.org/10.1016/j.ijthermalsci.2020.106607.

[25] S. Takarazawa, K. Ushijima, R. Fleischhauer, J. Kato, K. Terada, W.J. Cantwell, M. Kaliske, S. Kagaya, S. Hasumoto, Heat Mass Transf, in: Heat Mass Transf, 58, 2022, pp. 125–141, https://doi.org/10.1007/s00231-021-03083-0.

[26] M. Shahrzadi, M. Davazdah Emami, A.H. Akbarzadeh, Heat transfer in BCC lattice materials: conduction, convection, and radiation, Compos. Struct. 284 (2022), 115159, https://doi.org/10.1016/j.compstruct.2021.115159.

[27] J. Ernot, P.G. Verdin, H. Ahmad, P. Indge, Analytical and numerical predictions of the thermal performance of multi-layered lattice structures, Int. J. Heat Mass Transf. 145 (2019) 118752, https://doi.org/10.1016/j.ijheatmasstransfer.2019.118752.

[28] S. Yun, D. Lee, D.S. Jang, M. Lee, Y. Kim, Numerical analysis on thermo-fluid–structural performance of graded lattice channels produced by metal additive manufacturing, Appl. Therm. Eng. 193 (2021), 117024, https://doi.org/10.1016/j.applthermaleng.2021.117024.

[29] C. Hou, G. Yang, X. Wan, J. Chen, Study of thermo-fluidic characteristics for geometric-anisotropy Kagome truss-cored lattice, Chin. J. Aeronaut. 32 (2019) 1635–1645, https://doi.org/10.1016/j.cja.2019.03.023.

[30] T.M. Corbett, K.A. Thole, S. Bollapragada, Impacts of Pin Fin Shape and Spacing on Heat Transfer and Pressure Losses, J. Turbomach. 145 (2023) 10, https://doi.org/10.1115/1.4056092.

[31] T. Corbett, K.A. Thole, S. Bollapragada, Amplitude and Wavelength Effects for Wavy Channels, J. Turbomach. 145 (2022), 031011, https://doi.org/10.1115/1.4055612.

[32] Siemens, SimCenter STAR-CCM+, 2021.

[33] F. Nicoud, F. Ducros, Subgrid-scale stress modelling based on the square of the velocity gradient tensor, Flow Turbul. Combust. 62 (1999) 183–200, https://doi.org/10.1023/A:1009995426001.

[34] I. Kaur, P. Singh, Effects of inherent surface roughness of additively manufactured lattice frame material on flow and thermal transport, Int. J. Heat Mass Transf. 209 (2023), 124077, https://doi.org/10.1016/j.ijheatmasstransfer.2023.124077.

[35] L. Mazzei, R. Da Soghe, C. Bianchini, Calibration of a CFD methodology for the simulation of roughness effects on friction and heat transfer in additive manufactured components, in: Vol. 5B Heat Transf. — Gen. Interest Intern. Air Syst. Intern. Cool., American Society of Mechanical Engineers, Virtual, Online, 2021: p. V05BT13A010. 10.1115/GT2021-59603.

[36] S.B. Pope, Turbulent Flows, Cambridge University Press, Cambridge ; New York, 2000.

[37] A.G. Caket, C. Wang, M.A. Nugroho, H. Celik, M. Mobedi, Recent studies on 3D lattice metal frame technique for enhancement of heat transfer: discovering trends and reasons, Renew. Sustain. Energy Rev. 167 (2022), 112697, https://doi.org/10.1016/j.rser.2022.112697.

[38] G.W. Lowery, R.I. Vachon, The effect of turbulence on heat transfer from heated cylinders, Int. J. Heat Mass Transf. 18 (1975) 1229–1242, https://doi.org/10.1016/0017-9310(75)90231-8.

[39] N.K. Delany, N. Sorensen, Low-Speed Drag of Cylinders of Various Shapes, NACA, 1956. ntrs.nasa.gov/api/citations/19930083675/downloads/19930083675.pdf.

[40] W.S. Chiu, J.H. Lienhard, On Real Fluid Flow Over Yawed Circular Cylinders, J. Basic Eng. 89 (1967) 851–857, https://doi.org/10.1115/1.3609719.

[41] M.M. Zdravkovich, K.L. Stonebanks, Intrinsically nonuniform and metastableflow in and behind tube arrays, J. Fluids Struct. 4 (1990) 305–319, https://doi.org/10.1016/S0889-9746(05)80017-9.

[42] S. Ziada, A. Oengören, FLOW periodicity and acoustic resonance in parallel triangle tube bundles, J. Fluids Struct. 14 (2000) 197–219, https://doi.org/10.1006/jfls.1999.0259.